



Finite-size effects on the evolution of magnetic correlations and magnetocaloric properties of $\text{Pr}_{0.4}\text{Bi}_{0.2}\text{Sr}_{0.4}\text{MnO}_3$

Anita D. Souza¹ · Megha Vagadia² · Mamatha D. Daivajna¹

Received: 8 May 2021 / Accepted: 6 August 2021 / Published online: 18 August 2021
© The Author(s) 2021

Abstract

The effect of particle size reduction on the magnetic correlations of $\text{Pr}_{0.4}\text{Bi}_{0.2}\text{Sr}_{0.4}\text{MnO}_3$ nanoparticles prepared by *top-down* approach has been studied in detail. It was observed that as the milling time increases from 0 to 240 min, particle size decreases from 160 to 12 nm. Correspondingly it was observed that the ferromagnetic transition temperature (T_C) drops (264 to 213 K) and saturation magnetization (M_S) decreases (2.12–0.41 $\mu_B/\text{f.u.}$) while coercivity (H_C) shows a monotonous increase (0.18–1.5 kOe) as the particle size decreases due to increase in milling. The magnetic entropy change (ΔS) also decreases (2.41–0.24 J/kg·K) as particle size decreases indicating a strong correlation between magnetism and particle size. The metamagnetic M–H response of the bulk sample, which signifies the magnetic phase coexistence, is suppressed, and the nature of magnetic interactions demonstrates a transition from long range to short range. The observed characteristics emphasizes that with particle size reduction there is an increase in the surface disorder which can be explained by considering the core–shell model for the nanoparticles.

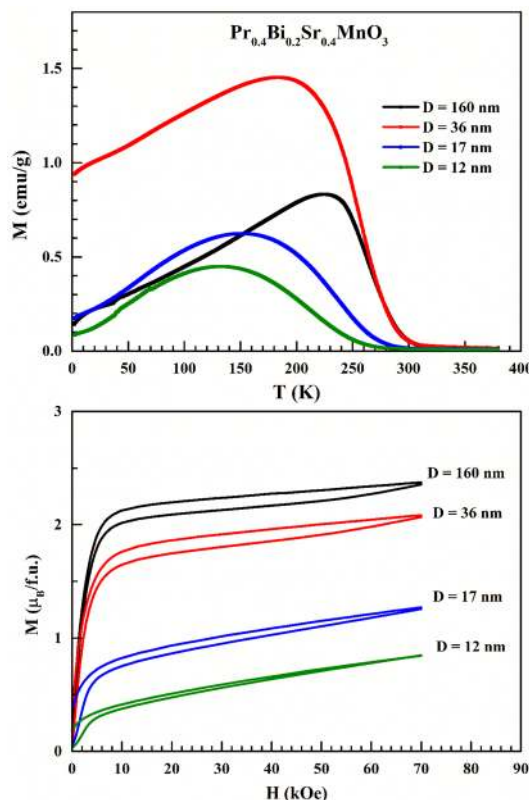
✉ Megha Vagadia
mvagadia@iiserb.ac.in; meghavagadia@gmail.com

✉ Mamatha D. Daivajna
mamatha.daijna@manipal.edu

¹ Department of Physics, Manipal Institute of Technology,
Manipal Academy of Higher Education, Manipal,
Karnataka 576104, India

² Department of Physics, Indian Institute of Science Education
and Research, Bhopal, Madhya Pradesh 462066, India

Graphic abstract



Keywords Magnetic properties · Magnetic phase coexistence · Magnetocaloric properties · Griffiths phase

1 Introduction

The understanding of magnetism at nanoscale is scientifically attractive not only because the quantum mechanical properties of the individual spins become significant, but also for the emergence of new phenomena from confinement and proximity, such as giant magnetoresistance (GMR), spintronics, and superparamagnetism [1–4]. The significant advances in the availability of strategies for the synthesis and characterization of materials have led to the massive interest in magnetic nanoparticles. Currently, magnetic nanostructures such as nanodisc, nanotubes, nanorods, nanowires, and nanocomposites are widely used as active components in magnetic refrigeration, magnetic diagnosis, drug delivery, catalysis, ferrofluids, sensors, energy storage, logic circuits, etc. [5–8]. Apart from the above, manipulating the size and shape of the nanostructures place them close to the biological entity such as gene, protein, and cell. This offers an upper hand for magnetic nanoparticles in biomedical applications such as magnetic hyperthermia, magnetic resonance imaging, tissue engineering, cell tracking, and bioseparation [9, 10]. Additionally, the large surface of the magnetic

nanostructures finds potential application in wastewater treatment as nanoabsorbent, energy harvesting, heat transfer, ferrofluids, photocatalysis, pigmentation, etc. [11–16].

The two key factors which dominate the magnetic properties of nanoparticles are the finite-size effects and the surface effects [5, 7]. Finite-size effects result from the quantum confinement of electrons such as single-domain limit and superparamagnetic limit, while the surface effects are related to symmetry breaking of the crystal structure at the boundary. The large fraction of atoms residing at the surface of the nanoparticle control the surface interface effects [4, 5, 7].

In perovskite rare earth manganites, nanoparticles display exotic features such as superparamagnetism, spin glass behaviour, low-field saturation magnetization, low-field magnetoresistance, and large coercivity which are different from their bulk counterparts [17, 18]. These striking characteristics make them suitable for application in magnetic hyperthermia, solid oxide fuel cells, magnetic memory devices, spintronic devices, and magnetic sensors [18]. The feasibility to tune the magnetic transition spread over a broad temperature range and the melting of the robust charge ordering (CO) state in the nanoparticles enable their

potential for magnetic refrigeration application [18–20]. Recently tailoring the ferroelectricity in hexagonal manganese thin films has been realized to be suitable for photovoltaic application [21].

Among rare earth manganites, $\text{Pr}_{1-x}\text{Sr}_x\text{MnO}_3$ has attracted extra attention owing to its resemblance to the prototype $\text{La}_{1-x}\text{Sr}_x\text{MnO}_3$ (LSMO). The parent compound PrMnO_3 is an antiferromagnetic (AFM) insulator with $T_N \approx 100$ K. Systematic replacement of Pr^{3+} by Sr^{2+} (i.e. $\text{Pr}_{1-x}\text{Sr}_x\text{MnO}_3$) changes the magnetic ground state and the system exhibits a second order paramagnetic (PM) to ferromagnetic (FM) transition for Sr^{2+} content $0.20 \leq x \leq 0.45$ [22–24]. In the present study, we focus our attention on $\text{Pr}_{0.6}\text{Sr}_{0.4}\text{MnO}_3$ (PSMO)-derived composition. PSMO is a room temperature metallic FM with $T_C = 310$ K, $T_{MI} = 260$ K and exhibits moderate magnetoresistance (MR) of 40% for $H = 80$ kOe [25, 26]. It is reported to undergo a structural transition from orthorhombic structure (space group $Pnma$) to monoclinic (space group $I2/a$) structure at $(T_S) = 88$ K [27]. It shows both normal and inverse magnetocaloric effect (MCE) in the same sample which is interesting from a practical application point of view as magnetic cooling can be achieved from both adiabatic magnetization and demagnetization in different temperature ranges [26, 28].

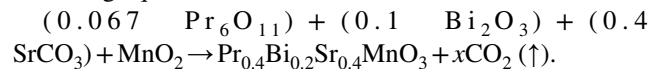
Contrary to PrMnO_3 , BiMnO_3 is an FM insulator with $T_C = 100$ K and crystallizes in a monoclinic structure [29, 30]. Sr^{2+} substitution for Bi^{3+} (i.e. $\text{Bi}_{1-x}\text{Sr}_x\text{MnO}_3$) reduces FM and induces charge ordered (CO) AFM for wide concentration of Sr^{2+} (i.e. $0.25 \leq x \leq 0.80$) [31, 32]. $\text{Bi}_{0.75}\text{Sr}_{0.25}\text{MnO}_3$ is a well-known CO-AFM showing the highest CO temperature, $T_{CO} = 625$ K among manganites which is robust and stable in an external field as high as 30 T [31, 33]. For $x = 0.40$, i.e. $\text{Bi}_{0.6}\text{Sr}_{0.4}\text{MnO}_3$ (BSMO), the compound shows a PM-to-AFM transition at $T_N = 150$ K and CO transition at $T_{CO} \approx 600$ K [31, 33]. Previous reports on Bi^{3+} -doped LaSrMnO_3 [34, 35], LaCaMnO_3 [36, 37], PrSrMnO_3 [38, 39] demonstrate a transition in the magnetic ground state from FM metallic to AFM insulating with competitive coexistence of FM and AFM clusters for intermediate concentration of Bi^{3+} [34–39]. Across the phase coexistence, the material exhibits a large MR ($\approx 100\%$) and MCE probably due to the melting of the CO state. In the partial doping concentration of Bi^{3+} , the system shows predominantly FM features with a systematic drop in T_C and net magnetization [34–39]. However, in the case of NdSrMnO_3 [40], NdCaMnO_3 [41], Bi^{3+} doping drives the system to be robust CO. The observed unusual behaviour of bismuth manganites is attributed to the presence of 6 *s* lone pair electrons in the outermost orbital of Bi^{3+} [42].

In view of the contrasting properties of PSMO and BSMO, in the present work, the effect of particle size reduction on the magnetic properties of 20% Bi^{3+} -doped $\text{Pr}_{0.6}\text{Sr}_{0.4}\text{MnO}_3$ (PSMO) is investigated in detail. 20% Bi^{3+}

when substituted in the case of FM $\text{La}_{0.7}\text{Sr}_{0.3}\text{MnO}_3$, retains dominant FM state both in the bulk form and in the nanoparticles [43]. However, in the case of FM LaCaMnO_3 [37, 44] and PrSrMnO_3 [39], AFM and FM phase separation has been noticed. Previous reports on Bi-substituted PSMO [38, 39, 45] reveal that for partial Bi^{3+} substitution T_C reduces and MR improves. For a higher concentration of Bi^{3+} , multiple magnetic interactions are observed [39]. In our previous studies on magnetic phase coexistence, the Bi^{3+} -substituted LSMO nanoparticles reveal an overall drop in net magnetization with size reduction while the metamagnetic M–H behaviour of the system remains significantly unaltered [46–48]. Contrary to that, we find in the present study the suppression in the metamagnetic M–H response with the decrease in particle size. Therefore, a detailed study of the present system was warranted, and we here present our analysis of X-ray diffraction studies and magnetization data discuss the results to reveal the role of particle size reduction on the structure, magnetization, magnetic correlations, and magnetocaloric effect (MCE) of $\text{Pr}_{0.4}\text{Bi}_{0.2}\text{Sr}_{0.4}\text{MnO}_3$ nanoparticles.

2 Experimental details

$\text{Pr}_{0.4}\text{Bi}_{0.2}\text{Sr}_{0.4}\text{MnO}_3$ (PB20SMO) nanoparticles have been prepared using a *top-down* approach in a two-step process. Initially, polycrystalline bulk samples were prepared by the solid-state reaction of Pr_6O_{11} , Bi_2O_3 , SrCO_3 , and MnO_2 (all 99.9% purity) weighed stoichiometrically according to the following equation.



These oxides were mixed thoroughly using agate mortar pestle with the help of isopropyl alcohol, to get a homogeneous mixture. The obtained mixture was calcined at 800 °C, 900 °C, and 1000 °C, respectively, for 24 h each with intermediate grinding. The powders were then pressed into rectangular pellets and were sintered at 1100 °C for 24 h.

In the second step, the pellets were then crushed into a fine powder and were subjected to high-energy planetary ball milling to prepare nanoparticles. The powders were taken in tungsten carbide jars of 50 ml volume along with 10 mm tungsten carbide balls such that the ball mass-to-sample mass ratio was maintained as 20:1. The ball milling was performed at the main disc speed of 300 rpm. The milling time was varied from 0 to 240 min, and a small quantity of sample was taken out at certain interval of time up to 240 min.

The obtained nanoparticles are characterized for their crystal structure and phase purity using room temperature X-ray diffraction (XRD) measurements taken on a M/s. Bruker D2 Phaser powder X-ray diffractometer with Cu-K α

radiation in the 2θ range of 20° – 80° with a step size of 0.02° . Magnetic measurements were taken on a M/s quantum design, superconducting quantum interference device (SQUID)-based vibrating sample magnetometer (VSM) in magnetic fields up to ± 70 kOe and in the temperature range 2–380 K.

3 Results and discussions

3.1 Room temperature X-ray diffraction

Figure 1a shows the room temperature XRD patterns of bulk and ball-milled PB20SMO samples. The XRD peaks display a systematic broadening with increase in milling time (t_m), suggesting reduction in particle size (D) and concomitant inducement of microstrain (ϵ) in the lattice. The full width at half maximum (FWHM) of the selected reflections, i.e. (1 2 1), (2 0 2), and (0 4 2), plotted as a function of t_m (Fig. 1b) shows a sudden rise in the value during the beginning of ball milling compared to higher t_m . This indicates a substantial drop in D occurs during the initial phase of ball milling compared to higher t_m .

To derive the structural parameters, the obtained XRD patterns have been subjected to Rietveld refinement method using the FullProf program [49]. Figure 1c shows the XRD profiles for selected PB20SMO- t ($t = 0, 20, 120$, and 240 min) along with the pattern calculated through Rietveld refinement method. The XRD patterns have been indexed considering the orthorhombic structure in $Pnma$ space

group. As all the Bragg peaks could be indexed using this structure, contamination in the sample during ball milling can be ruled out. This indicates that all the samples studied here are of single phase. The unit cell parameters and reliability values of Rietveld refinement are summarized in Table 1.

For better estimation of D and ϵ using XRD, the instrumental resolution file (IRF) was obtained by measuring a NIST standard sample (corundum), before starting the Rietveld refinement of PB20SMO. For subsequent PB20SMO samples, only the quantities influenced by the sample properties were refined. The TCH pseudo-Voigt peak shape function [50] was considered for both standard and our samples. On supplying the IRF file during Rietveld refinement, Fullprof generates a volume average of particle size (D) and microstrain (ϵ) through the integral breadth method in a microstructure file (*.mic file) [50]. Figure 2 shows the variation in D and ϵ as a function of t_m . A sudden drop in the D has been noticed as the t_m changes from 0 to 60 min while the ϵ exhibits monotonous increment up to 150 min of ball milling and then tends to saturate. The substantial drop in D could be attributed to the enhanced rate of dislocation densities (δ) and defects induced due to the constant collision between the sample mass and balls with the walls of the jar [51, 52]. From D , an estimation of δ can be obtained from the relation $\delta = \frac{1}{D^2}$ [53]. Inset in Fig. 2 shows the variation in δ with t_m . As t_m increases from 0 to 240 min, δ shows substantial increase from 10^{13} to 10^{15} lines/m². Also, since the dimension of the feed size before ball milling is larger compared to after each milling

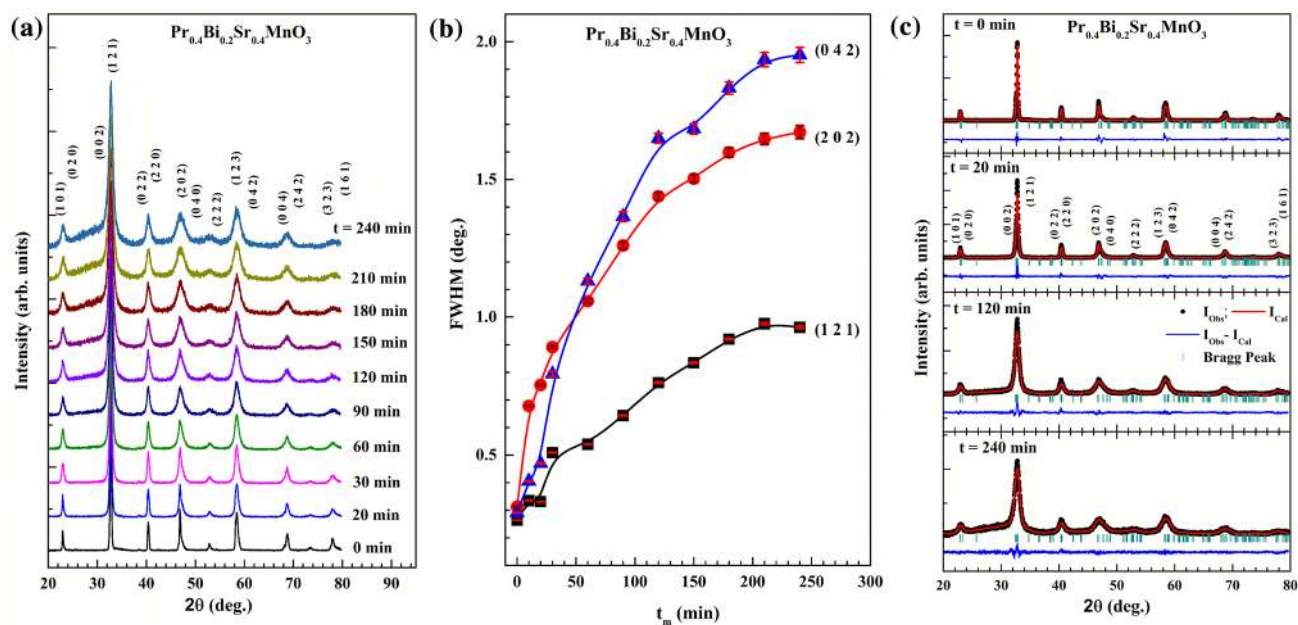
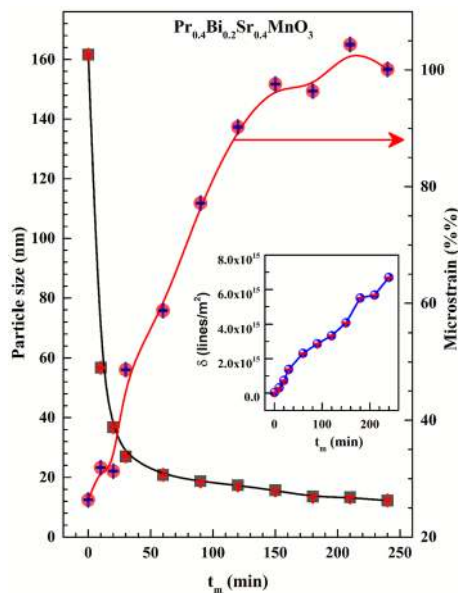


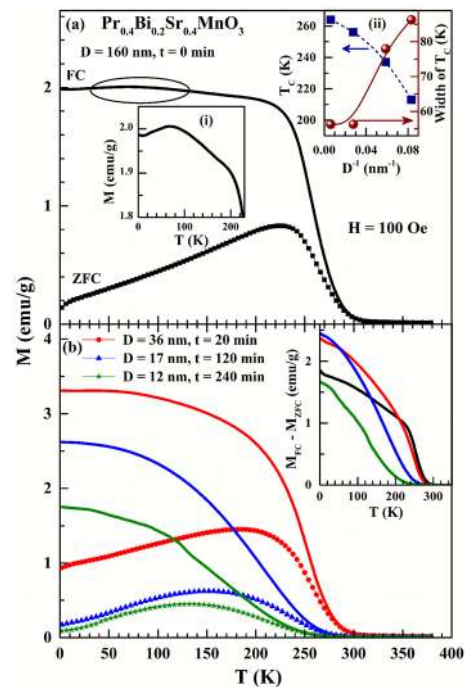
Fig. 1 a Room temperature XRD patterns of bulk and ball-milled PB20SMO. b A plot showing the variation in FWHM of (1 2 1), (0 4 2), and (2 0 2) diffraction peaks for bulk and ball-milled PB20SMO. c Rietveld refined XRD patterns of PB20SMO- t ($t = 0, 20, 120$, and 240 min)

Table 1 Rietveld refined unit cell parameters and reliability values of Rietveld refinement of X-ray diffraction patterns for PB20SMO-t refined using orthorhombic structure, space group $Pnma$

PB20SMO-t	t=0 min	t=20 min	t=120 min	t=240 min
a (Å)	5.46801 (27)	5.46894 (27)	5.48661 (178)	5.48438 (238)
b (Å)	7.68497 (34)	7.67849 (25)	7.64509 (80)	7.63690 (117)
c (Å)	5.49744 (25)	5.50121 (26)	5.50932 (196)	5.51168 (263)
V (Å ³)	231.011 (19)	231.014 (18)	231.092 (114)	230.849 (153)
R_p	14.5	11.0	9.15	7.52
R_{wp}	20.0	14.5	11.8	9.70
R_{exp}	11.48	9.01	9.44	9.06
χ^2	3.05	2.59	1.55	1.14
Bragg R Factor	8.22	5.72	3.64	2.54
Particle size (D) (nm)	160	36	17	12
Microstrain (ϵ) $\times 10^{-4}$	26.33	31.26	90.21	100.09
Dislocation density $\delta = \frac{1}{D^2} \times 10^{15}$ (lines/m ²)	0.039	0.771	3.460	6.944
Degree of crystallinity (%)	92.64	90.91	74.46	66.01

**Fig. 2** The variation of particle size and microstrain is shown as a function of milling time for PB20SMO. Inset shows the variation in dislocation density with milling time

time, a huge drop in D and a rise in ϵ is witnessed during the initial phase of ball milling. Further, the degree of crystallinity (DC) has been estimated using the relation $DC = \frac{\text{Area of crystalline peaks}}{\text{Area of all peaks (crystalline + amorphous)}}$. DC decreases from 92 to 66% as t_m increases (Table 1). Thus, based on the estimated D from XRD, four samples obtained after $t = 0, 20, 120$, and 240 min of ball milling having particle size $D = 160, 36, 17$, and 12 nm, respectively, were chosen to study, in detail, the influence of particle size reduction on the magnetic properties.

**Fig. 3** A plot of temperature-dependent dc magnetization for **a** bulk and **b** ball-milled PB20SMO in an applied field of 100 Oe. Inset (i) in **3 a** shows the enlarged view of low-temperature hump. Inset (ii) in **3 a** shows variation in T_C and width of dM/dT as a function of D^{-1} . The line connecting the points is a guide to eyes. Inset in **3 b** shows temperature variation of $M_{FC} - M_{ZFC}$

3.2 Magnetization studies

Figure 3 shows the dc magnetization plots for PB20SMO- D samples ($D = 160, 36, 17, 12$ nm) in the temperature range of 3–380 K in an applied field of 100 Oe. The magnetization has been recorded under zero field-cooled (ZFC) and field-cooled (FC) state of the samples. All samples show a

well-defined PM-to-FM transition (T_C) which drops from 264 K for $D=160$ nm to 210 K for $D=12$ nm (inset (ii) in Fig. 3a). Compared to PSMO which has $T_C=308$ K [28, 54], 20% Bi^{3+} substitution reduces the T_C to 264 K. Also, the low-temperature structural transition which was seen as a drop in ZFC and FC curve for PSMO [26, 28] is suppressed with Bi^{3+} substitution. However, the bulk PB20SMO-160 ($D=160$ nm) sample shows a hump in FC at $T < 200$ K which could be attributed to the disordered antiferromagnetic (AFM) interactions in the system. Similar low-temperature hump in FC curve has been noticed in case of $\text{La}_{0.7-x}\text{Bi}_x\text{Sr}_{0.3}\text{MnO}_3$ ($x=0.30$ and 0.35) [46, 48, 55]. The decrease in T_C with Bi^{3+} substitution can be explained considering the increase in unit cell volume. As seen from the XRD analysis, the unit cell volume increases from 229.214 to 231.011 \AA^3 as x changes from 0 to 0.20 [54]. This elongates the Mn–O–Mn chains, thus reducing the hopping of e_g electrons. The double exchange coupling weakens, thereby resulting in the decrease of T_C . Also, the highly covalent 6s lone pair character of Bi^{3+} is expected to create localization of electrons around the Bi^{3+} -rich region which leads to AFM coupling, thereby decreasing the FM character of PSMO.

Further, the sharp magnetic transition recorded for the bulk sample broadens with the decrease in D which can be seen as the increase in the FWHM of dM/dT curve (inset (ii) in Fig. 3a). This may be due to the weak magnetic interaction among the spins on the surface of the nanoparticles. Also, a large bifurcation between ZFC and FC curves noticed in all samples specifies the presence of inhomogeneity in the system. The strength of the inhomogeneity can be quantified as $M_{\text{FC}} - M_{\text{ZFC}}$ (inset in Fig. 3b) which is higher for PB20SMO-36 and PB20SMO-17 samples.

The high-temperature inverse magnetic susceptibility (χ^{-1}) has been analysed using the Curie–Weiss (CW) law [56], $\chi = \frac{C}{T - \theta_p}$, C is Curie's constant, and θ_p is Curie–Weiss temperature. Figure 4 shows the χ^{-1} vs T plots for PB20SMO- D . From the slope of the linear fit in the temperature range $310 < T < 380$ K, the values of θ_p have been determined. Inset in Fig. 4 shows the θ_p vs D^{-1} plot. The positive values of θ_p demonstrate the dominant FM interactions in the system. With a decrease in D , the θ_p value decreases suggest a weakening of FM interaction with size reduction. Additionally, it is interesting to note that all samples show a deviation from the CW behaviour exhibiting a downturn, below a certain temperature (T_G) in each sample's case. This may be accounted as the presence of short-range FM correlations above T_C . Most reports assign this anomaly to the Griffith's like singularity in the system [57–60] while some literature suggests the presence of FM polarons above T_C could result in $\chi^{-1}(T)$ downturn [61–63]. In general, the existence of GP like behaviour is characterized by a downturn in $\chi^{-1}(T)$, which is sharp for lower applied fields and subdue with

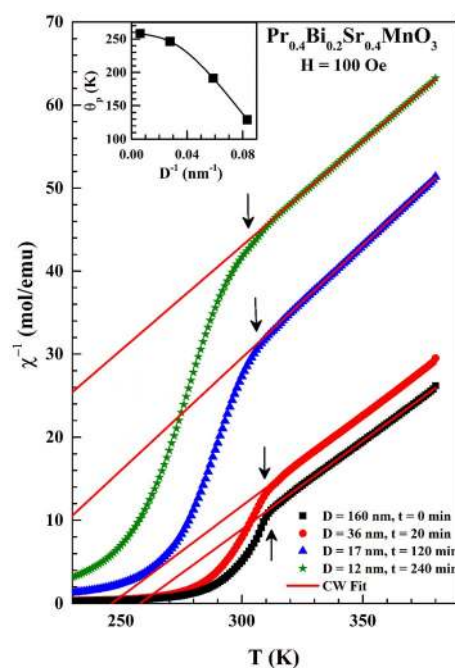


Fig. 4 Temperature evolution of inverse magnetic susceptibility for PB20SMO- D ; the solid line indicates the linear fit to the CW law. Inset **b** shows the variation in θ_p as a function of D^{-1}

an increase in the magnitude of applied magnetic field. Also, the low field χ^{-1} shows a temperature dependence given by the power law [57],

$$\chi^{-1} \propto (T - T_C^R)^{(1-\lambda)} \quad 0 \leq \lambda \leq 1 \quad (1)$$

where T_C^R is the critical temperature of a random ferromagnet and the exponent λ determines the deviation from CW law. The temperature at which $\chi^{-1}(T)$ deviates from linearity is known as Griffith's temperature, T_G . The T_G in the present case decreases with a decrease in particle size. Figure 5 shows the χ^{-1} vs T plots in different applied magnetic fields for PB20SMO- D . A systematic softening of the downturn has been noticed with an increase in the magnitude of applied magnetic field. This may be understood as in higher applied fields the magnetic contribution from PM matrix enhances and dominates the embedded FM clusters, hence driving towards linear variation in χ^{-1} vs T . Using the procedure described in Ref [57], the value of λ has been estimated from the plot of χ^{-1} vs $[(T/T_C^R) - 1]$ in double logarithmic scale (inset in each panel of Fig. 5). The slope of the linear fit gives the value of λ tabulated in Table 2. The estimated value of λ is in good agreement with the reported literature [57–60], thereby suggesting the applicability of GP model to explain the deviation in $\chi^{-1}(T)$. Also, the magnitude of λ is found to increase with particle size reduction implying the enhancement in the strength of GP like singularity. On the contrary, Souza et al. [61] suggested that GP like treatment

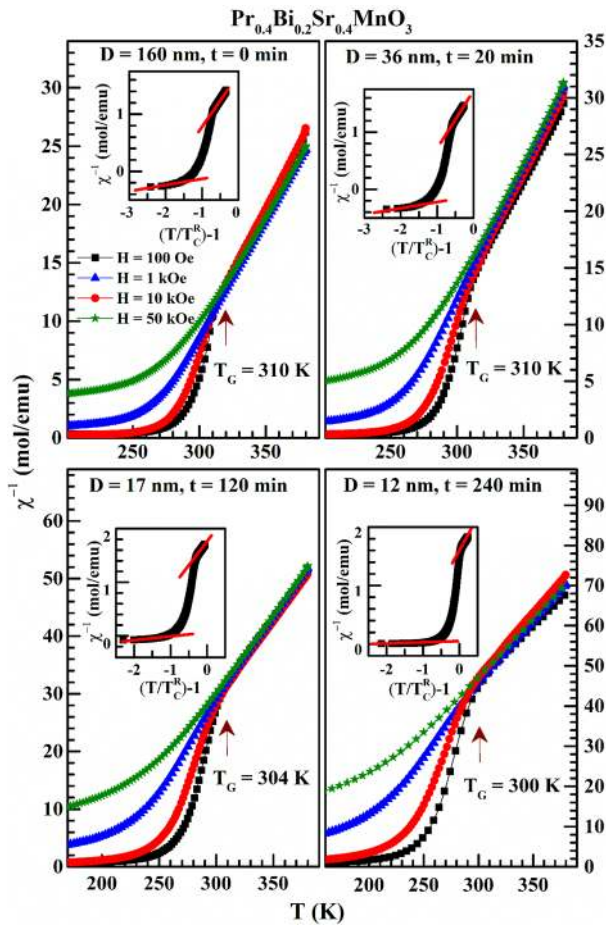


Fig. 5 A plot of temperature evolution of inverse magnetic susceptibility in different magnetic fields for PB20SMO. Inset in each panel shows inverse susceptibility versus $[(T/T_G)^n - 1]$ in double logarithmic scale and solid line represent the linear fit

Table 2 Values of T_C , θ_p , T_G , λ , M_S , and other calculated microstructural parameters for bulk and ball-milled PB20SMO samples

Sample (PB20SMO-D)	D = 160	D = 36	D = 17	D = 12
T_C (K)	264	256	237	213
θ_p (K)	256	246	191	129
T_G (K)	310	310	304	300
λ_{PM}	0.02	0.09	0.06	0.04
λ_{GP}	0.86	0.86	0.92	0.95
M_S —3 K ($\mu_B/f.u.$)	2.12 (02)	1.82 (001)	0.87 (002)	0.41 (003)
a (3 K, kOe)	0.25 (0.01)	0.26 (0.01)	1.53 (0.04)	1.82 (0.07)
b (3 K, kOe ²)	4.13 (0.06)	2.79 (0.07)	2.47 (4)	2.71 (0.21)
$\chi_p \times 10^{-5}$ (3 K)	351 (2)	388 (2)	593 (2)	636 (6)
$K \times 10^5$ (3 K) erg/cm	2.09	1.47	0.67	0.33
Shell thickness (t) (nm)	—	1.47	2.53	2.62

for accounting the $\chi^{-1}(T)$ downturn is inappropriate and proposed the presence of FM polarons, intrinsic to manganites due to structural and chemical disorder to be responsible for $\chi^{-1}(T)$ deviation from CW behaviour. Later, Rozenberg et al. [64, 65] and Aga Shahee et al. [66] supported the above hypothesis. Since conductivity in manganites above T_{MI} is accounted by the hopping of small polarons, it appears as if both the proposed models hold. However, the magnitude of resistivity and polaron activation energy E_a of a ferromagnetic manganite is found to increase with a decrease in D [67–69], thus suspecting the applicability of the FM polarons hypothesis.

To gain deeper insights into the magnetic interactions, field-dependent isothermal magnetization loops were recorded for PB20SMO-D at different temperatures (Fig. 6a–d). For PB20SMO-160, the M–H behaviour at 300 K is nonlinear and unsaturated suggesting the presence of weak magnetic interactions in the system. On lowering the temperature to $T < T_C$, i.e. 200 K, the M–H response shows a significant spontaneous moment (M_0) with unsaturated magnetization suggesting the coexistence of FM and AFM interactions in the system. At $T = 100$ K and 50 K, the M–H

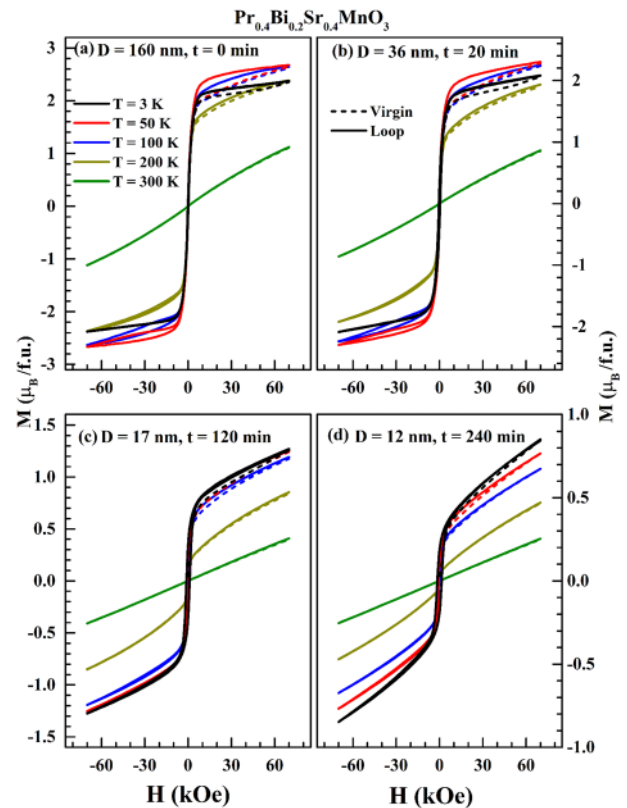


Fig. 6 Field-dependent magnetization plots for PB20SMO-D, **a** $D = 160$ nm, **b** $D = 36$ nm, **c** $D = 17$ nm, and **d** $D = 12$ nm at different temperatures

loops represent distinct behaviour with open loops along the positive and negative field sweep. The magnetization in the virgin loop remains unsaturated even in the field as high as 70 kOe with notable spontaneous moment signifying the alignment of residual FM domains parallel to the applied magnetic field. In the reverse field sweep (demagnetization curve), the sample remains in a high state down to 10 kOe and then rapidly drops to zero at $H=0$ kOe. In the negative field sweep, a response similar to the positive field sweep has been noticed; however, the area under the loop along with the forward and reverse field sweep is less compared to the positive field sweep. The observed M – H response implies the presence of metamagnetic magnetization with the ramping field. This suggests field-induced AFM-to-FM transition in the system. At $T=3$ K, a clear step like feature has been observed in the virgin curve at critical field $H_{CR}=50$ kOe. Along the demagnetization path, the system remains in a high magnetic state down to 9 kOe field and then drops to zero at zero field. When the field is increased in the negative direction, the magnetization curve is similar to the demagnetization curve of the positive field and follows a similar pathway with further field sweep. This indicates that the field-induced transition from the AFM to FM state is irreversible and the induced FM phase is stable at this temperature. The net magnetization at 3 K is less compared to that at 50 K and 100 K and indicates an increase in the volume fraction of AFM interactions at 3 K.

For PB20SMO-36, the recorded magnetization with the ramping field is similar to that of PB20SMO-160 but a small drop in the open-loop area has been noticed. In the case of PB20SMO-17 and PB20SMO-12, the M – H is highly unsaturated signifying the increased surface disorder that leads to the reduced magnetic interaction. Also, it is interesting to note that the difference between the virgin curve and loop which was clearly identified in the bulk sample tend to merge in ball-milled sample implying the increase in the strength of AFM interaction or surge in the surface disorder due to ball milling that brings down the strength of FM interaction in the nanoparticles. Further, the net magnetization has been found to systematically increase with a decrease in temperature contrary to PB20SMO-160 and PB20SMO-36.

Figure 7 shows the temperature evolution of (a) saturation magnetization (M_S) and (b) coercivity (H_C). On lowering the temperature from 300 K, an overall increase in the value of M_S and H_C is noticed. The elevation in M_S with a decrease in T corroborates the PM-to-FM transition in all the samples while a small drop in M_S at a lower temperature for $D=160$ and 36 nm ratifies the hump recorded in the FC curve below $T=200$ K for PB20SMO-160 (inset (ii) in Fig. 3a). The H_C values plotted as a function D (inset in Fig. 7b) display a rise with a drop in D due to the increased surface anisotropy because of the lattice strain and broken bonds as the D comes down [70]. In general,

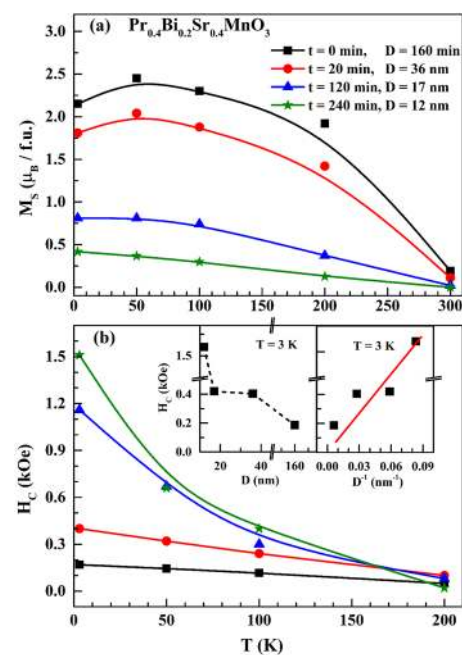


Fig. 7 Temperature evolution **a** M_S and **b** H_C for bulk and ball-milled PB20SMO. Inset in **b** shows the variation in H_C as a function of particle size (D) and D^{-1} . Solid line represents the linear fit

with a decrease in D , H_C increases and attains a maximum value for a critical particle size D_C where nanoparticles show a transition from multidomain to single-domain state. For further decrease in D , H_C drops. Inset in Fig. 7b shows the variation in H_C vs D^{-1} fitted to $H_C = m + n/D$, where m and n are constants. Linear variation in H_C vs D^{-1} (inset in Fig. 7b) suggests the multidomain nature of the nanoparticles [43, 71].

The law of approach to saturation (LAS) fit [72],

$$M = M_S \left(1 - \frac{a}{H} - \frac{b}{H^2} \right) + \chi_p H \quad (2)$$

given to the demagnetization curves in the first quadrant provide more insights into the magnetic behaviour. The term M_S in the above relation refers to the saturation magnetization, a/H corresponds to the structural defects while b/H^2 is related to the uniaxial magneto-crystalline anisotropy given as [73] $K = \sqrt{\frac{15}{4}} b M_S^2$ (erg/cm) and $\chi_p H$ is the high field susceptibility. Figure 8 shows the LAS fit given to the M – H curves at 3 K and the fitting parameters are summarized in Table 2. A rise in the a/H values specifies an increase in the structural defects due to ball milling. The estimated K values are of the order 10^5 erg/cm 3 and decrease with particle size reduction due to disorder in the core of the nanoparticles. Further a substantial drop in M_S from 2.1 $\mu_B/f.u.$ to 0.2 $\mu_B/f.u.$ has been noticed with a drop in D (Fig. 9). M_S plotted as a function of D^{-1} (inset in Fig. 9) shows a linear variation

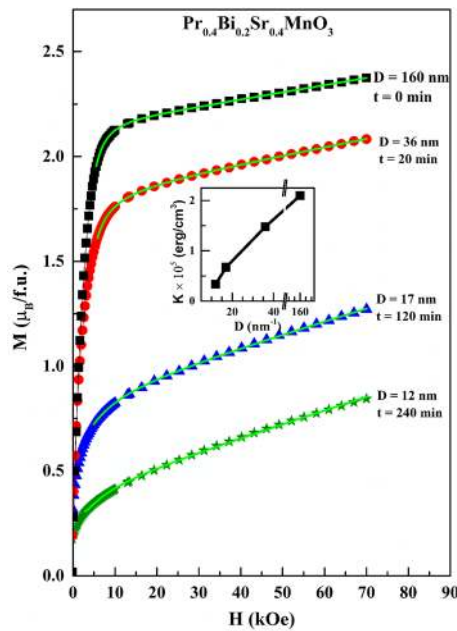


Fig. 8 M–H loops for bulk and ball-milled PB20SMO at 3 K. Solid line represents the fit given to the law of approach to saturation. Inset shows the variation in K as a function of D^{-1}

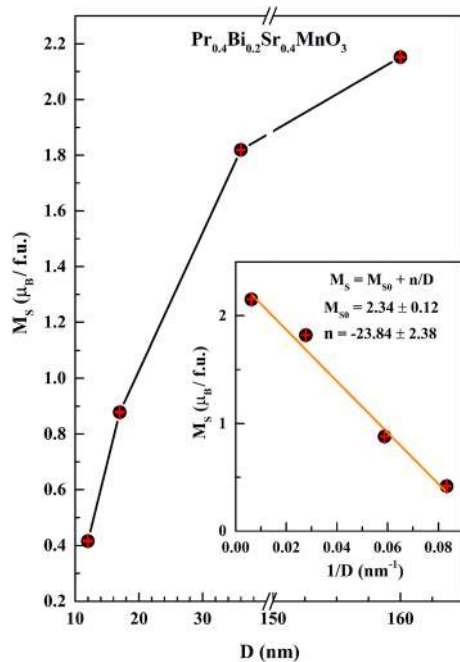


Fig. 9 A plot showing variation of M_S as a function of particle size (D). Inset shows the linear fit (solid line) given to M_S vs D^{-1}

specifying a strong impact of particle size on the M_S of the sample.

The range of magnetic interaction with particle size reduction can be interpreted from the M^2 vs H/M (i.e.

Arrott's plots) [57, 66]. If the linear interpolation of the high-field-magnetization region of M^2 vs H/M yields a positive slope, it represents the presence of spontaneous moment with long-range FM order while the negative slope represents short-range FM correlations in the system. As shown in Fig. 10, the intercept value for PB20SMO-160 and PB20SMO-36 is negative at $T = 300 \text{ K} > T_C$ and positive for $T \leq 200 \text{ K} < T_C$, demonstrating that the magnetic interactions above T_C are short-ranged while those below T_C the system exhibit long-range FM order. Similarly, for PB20SMO-17, the intercept has negative value at $T > 200 \text{ K}$ and transforms to be positive $T < 100 \text{ K}$ signifying a crossover in the range of FM interactions across magnetic ordering. However, for PB20SMO-12, the intercept is negative at all temperatures demonstrate the FM interactions to be short-ranged due to increased surface disorder because to ball milling.

The magnetic entropy change ΔS has been determined from iso-field magnetization using Maxwell's thermodynamic relation [74],

$$\Delta S(T, H) = S_M(T, H) - S_M(T, 0) = \int_0^H \left(\frac{\partial M}{\partial T} \right)_H dH \quad (3)$$

where M is the magnetization, H is the applied magnetic field, and T is the temperature. According to Maxwell relation, the change in magnetic entropy upon application of magnetic field is related to magnetization with respect to the temperature through

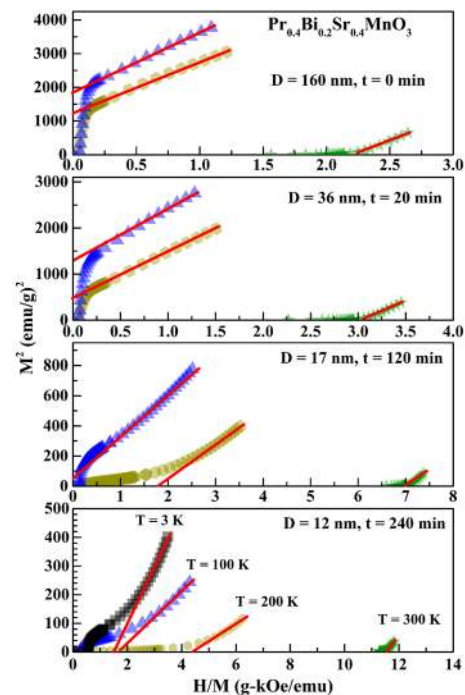


Fig. 10 A plot of M^2 vs. H/M (Arrott's plot) for PB20SMO- D

$$\left(\frac{\partial S}{\partial H}\right)_T = -\left(\frac{\partial M}{\partial T}\right)_H$$

Most frequently magnetization isotherms recorded across the T_C/T_N and specific heat measurements are used to estimate the ΔS values [74]. However, some recent reports suggest the estimation of ΔS from iso-field magnetization [75, 76]. A close overlap in the estimation of ΔS from isothermal and iso-field magnetization validates the application of the latter approach to estimate the MCE. Figure 11 a-d shows the variation of ΔS as a function of temperature in different applied fields (i.e. $H = 10$ kOe and 50 kOe). As expected, a large change in ΔS has been observed in the vicinity of T_C . The bulk PB20SMO shows a maximum entropy change ΔS_M of 2.43 J/kg-K for $H = 50$ kOe which drops to 0.24 J/kg-K as particle size reduces (table. 3) along with broadening of ΔS curve. The relative cooling power (RCP) defined as $RCP = \Delta S_M \times \delta T_{FWHM}$, where δT_{FWHM} is the full width half maximum of ΔS curve, also drops with a decrease in the particle size (table 3).

A sudden variation in ΔS across T_C could be accounted for by considering the change in magnetization and the

Table 3 Values of ΔS_M , δT_{FWHM} , and RCP for different applied magnetic fields for bulk and ball-milled PB20SMO

Sample	H (kOe)	ΔS_M (J/Kg K)	δT_{FWHM} (K)	RCP (J/Kg)
PB20SMO-120	1	0.015	48.67	0.73
	10	0.426	61.27	26.10
	50	2.410	78.89	190.01
PB20SMO-36	1	0.011	67.14	0.73
	10	0.269	79.73	21.44
	50	1.580	99.03	156.46
PB20SMO-17	1	0.003	113.46	0.34
	10	0.081	121.26	9.70
	50	0.491	141.61	69.38
PB20SMO-12	1	0.001	126.99	38.99
	10	0.037	139.98	5.17
	50	0.244	159.81	38.99

spin–lattice coupling across the magnetic ordering temperature [74]. The variation in the Mn–O–Mn bond angle and Mn–O bond length with temperature results in the volume change, thereby influencing the ΔS values. A comparison of the obtained ΔS_M with few reported studies is summarized in table 4 [77–84]. The ΔS_M value in the present study is less compared to PSMO which indicates that Bi^{3+} addition suppresses the net magnetization of the system.

From the above results, it can be noticed that with an increase in t_m , the dislocation density and microstrain increase while the degree of crystallinity drops. Correspondingly a decrease in T_C , M_S , K , and ΔS has been observed while H_C values display a monotonous increase. Also, a transition in the range of magnetic interactions from long range to short range has been noticed. A similar variation in the magnetic properties with a decrease in particle size has been previously reported in the case of manganites [28, 71, 73, 85–88] and other oxides [89–92]. The observed characteristic could be accounted for by considering the core–shell structure of the nanoparticles [93], according to which each nanoparticle has a FM/AFM grain surrounded by a non-magnetic shell comprised of broken bonds and randomly oriented magnetic spins.

Assuming the net magnetization of the shell to be zero, an estimate of shell thickness (t) can be attained from the relation [94],

$$t = \frac{D}{2} \left(1 - \left(\frac{M_{S(\text{Nano})}}{M_{S(\text{Bulk})}} \right)^{1/3} \right) \quad (4)$$

where D is the particle size, $M_{S(\text{Bulk})}$ and $M_{S(\text{Nano})}$ corresponds to the saturation magnetization of bulk and nanoparticles, respectively. The $M_{S(\text{Bulk})}$ value is obtained from the intercept of M_S vs D^{-1} plot (inset in Fig. 10). The estimated obtained values of t are tabulated in Table 2. Figure 12

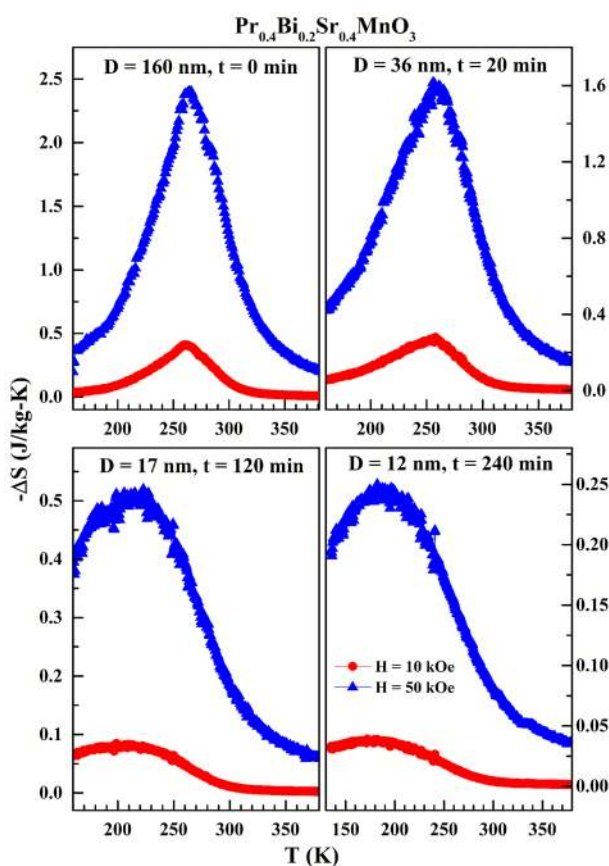
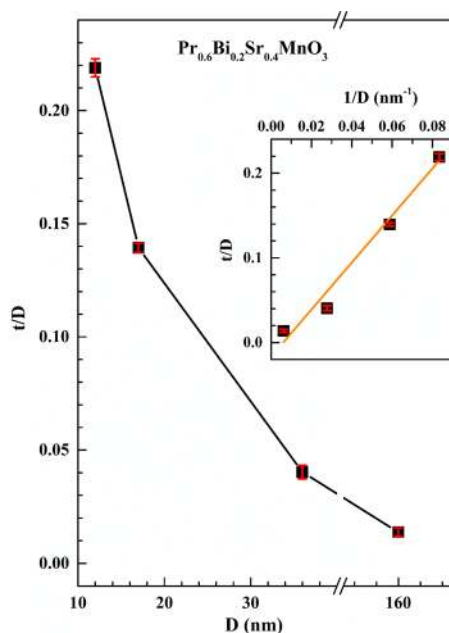


Fig. 11 Variation in magnetic entropy change (ΔS) plotted as a function of temperature for bulk and ball-milled P20SMO at different applied magnetic field ($H = 10, 50$ kOe)

Table 4 A comparison of ΔS_M and RCP values for different samples

Compound	T_C (K)	H (kOe)	ΔS_M (J/kg-K)	RCP (J/kg)	Ref
$\text{Pr}_{0.55}\text{Sr}_{0.45}\text{MnO}_3$	300	30	1.71	143.64	77
$\text{Pr}_{0.6}\text{Sr}_{0.4}\text{MnO}_3$	321	25	2.3	35.5	78
$\text{Pr}_{0.6}\text{Sr}_{0.4}\text{MnO}_3$	310	60	3.9	56	79
$\text{La}_{0.37}\text{Bi}_{0.3}\text{Ba}_{0.33}\text{MnO}_3$	229	50	3.42	260	80
$\text{La}_{0.47}\text{Bi}_{0.2}\text{Ba}_{0.33}\text{MnO}_3$	270	50	3.88	236	80
$\text{La}_{0.75}\text{Bi}_{0.05}\text{Ba}_{0.20}\text{MnO}_3$	300	40	3.41	180.16	81
$\text{La}_{0.5}\text{Bi}_{0.3}\text{Sr}_{0.08}(\text{Ca}_{0.55}\text{Ba}_{0.45})_{0.12}\text{MnO}_3$	140	20	1.62	136	82
$\text{La}_{0.7}\text{Sr}_{0.1}\text{Bi}_{0.2}\text{MnO}_3$	195	10	0.51	-	83
$\text{La}_{0.7}\text{Bi}_{0.3}\text{MnO}_3$	115	10	0.47	-	83
$\text{Pr}_{0.7}\text{Bi}_{0.1}\text{Sr}_{0.2}\text{MnO}_3$	140	50	3.11	196.39	84
$\text{Pr}_{0.8}\text{Sr}_{0.2}\text{MnO}_3$	210	50	5.41	197.95	84
$\text{Pr}_{0.4}\text{Bi}_{0.2}\text{Sr}_{0.4}\text{MnO}_3$, D = 160 nm	264	50	2.41	190.01	Present work
$\text{Pr}_{0.4}\text{Bi}_{0.2}\text{Sr}_{0.4}\text{MnO}_3$, D = 36 nm	256	50	1.580	156.46	Present work

**Fig. 12** Variation in t/D as a function of particle size (D). Inset shows the linear fit given to t vs D^{-1}

shows the variation of t/D (i.e. shell thickness/particle size) as a function of D . The t/D ratio increases monotonously with a drop in D . A linear dependence of t/D with D^{-1} suggests a direct impact of size reduction on the thickness of the non-magnetic shell that strongly controls the magnetic properties of the nanoparticles.

Since it has been well understood that with a decrease in D , the surface effects dominate compared to the core. The growth in dislocation density, vacancies, lattice defects, and low crystallinity adds to the surface defects which increases the separation between the FM core. This, in turn, reduces the magnetic interaction among them resulting in the drop

of net magnetization, T_C and ΔS_M with broad magnetic transitions. However, the metamagnetic magnetization loops noticed for bulk and ball-milled PB20SMO demonstrate the observed behaviour to be a characteristic of magnetic interaction among the cores. Since it has been well established that PSMO is a metallic FM [12] and BSMO is a CO-AFM [16], PB20SMO represents a solid solution in both parent phases, thus showing the magnetic state of both phases. Similar coexistence of FM and AFM phases has been reported in case of Bi-substituted LaCaMnO₃ [22, 34], LaSrMnO₃ [20, 41], NdSr/CaMnO₃ [25, 26] for a particular concentration of Bi³⁺. Even though Bi³⁺ is diamagnetic and the Mn³⁺/Mn⁴⁺ concentration is unaltered with Bi³⁺ substitution, the presence of 6s lone pair electrons of Bi³⁺ leads to the localization of charges across the Bi–O bonds. The antiparallel spin orientation between localized electrons and Mn³⁺/Mn⁴⁺ results in AFM superexchange coupling between Mn–O–Mn chains around Bi³⁺-rich regions, thereby driving the system towards AFM.

Further, the scientific conflict in assigning the sharp downturn observed in χ^{-1} (T) to either GP like singularity or the presence of FM polarons demands the presence of quenched disorder in the system [43–53]. Generally, in most of the manganites, A-site substitution that leads to the structural distortion due to the tilting of MnO₆ octahedra is expected to be the cause of quenched disorder while some reports suggest the competitive coexistence of the FM and AFM phases [44] and the magnetic interactions among the different magnetic ions due to B-site substitution [43] also results in quenched disorder. In the present case, the tilting of MnO₆ octahedra along with FM and AFM phase coexistence due to Bi³⁺ ions could be considered as the source of quenched disorder in bulk PB20SMO. Additionally, the broken Mn–O–Mn network due to ball milling also adds to the quenched disorder in PB20SMO nanoparticles. The local FM fluctuations resulted from the random spatial variation

in the magnetic exchange interactions due to particle size reduction result in the formation of short-range FM domains embedded in the PM matrix.

4 Conclusions

Systematic analysis of the magnetization data has been carried out to understand the role of particle size reduction on the magnetic correlations and magnetocaloric properties of $\text{Pr}_{0.4}\text{Bi}_{0.2}\text{Sr}_{0.4}\text{MnO}_3$. As the particle size decreases from 160 to 12 nm, T_C drops from 264 to 213 K along with a drastic reduction in the net magnetization from 2.12 to 0.41 $\mu_B/\text{f.u.}$ and ΔS_M from 2.43 to 0.24 J/kg·K. Correspondingly a suppression in the metamagnetic M–H loops has been observed which suggests a reduced magnetic interaction among the nanoparticles. The observed properties can be explained due to the formation of a non-magnetic shell around the FM/AFM core. Additionally, a sharp downturn noticed in the inverse susceptibility suggests the presence of short-range FM correlations above T_C .

Acknowledgements AD is indebted to the Department of Science and Technology, India, for financial support through the INSPIRE Fellowship (IF 170553). MV acknowledges the Department of Science and Technology, India, for the INSPIRE faculty award (DST/INSPIRE/04/2017/003059). The authors are thankful to Dr. S. Rayaprol (UGC-DAE-CSR, Mumbai) for fruitful discussions, M. Venugopal (UGC-DAE-CSR, Mumbai) for help in high-energy planetary ball milling and XRD measurements, and Mr. Manoj Prajapat for help in magnetic measurements.

Author's contribution ADS carried out conceptualization, formal analysis, and investigation, and wrote the original draft. MV performed validation, resources, writing, reviewing, and editing. MD was involved in supervision, writing, reviewing, and editing.

Funding Open access funding provided by Manipal Academy of Higher Education, Manipal.

Data availability The data set analysed in the current study could be available from the corresponding author on reasonable request.

Declarations

Conflict of interest The authors declare that they have no conflict of interests.

Open Access This article is licensed under a Creative Commons Attribution 4.0 International License, which permits use, sharing, adaptation, distribution and reproduction in any medium or format, as long as you give appropriate credit to the original author(s) and the source, provide a link to the Creative Commons licence, and indicate if changes were made. The images or other third party material in this article are included in the article's Creative Commons licence, unless indicated otherwise in a credit line to the material. If material is not included in the article's Creative Commons licence and your intended use is not permitted by statutory regulation or exceeds the permitted use, you will

need to obtain permission directly from the copyright holder. To view a copy of this licence, visit <http://creativecommons.org/licenses/by/4.0/>.

References

1. M.N. Baibich, J.M. Broto, A. Fert, F. Nguyen Van Dau, F. Petroff, P. Etienne, G. Creuzet, A. Friederich, J. Chazelas, Giant magnetoresistance of (001) Fe/(001) Cr magnetic superlattices. *Phys. Rev. Lett.* **61**, 2472 (1988)
2. I. Žutić, J. Fabian, S.D. Sarma, Spintronics: Fundamentals and applications. *Rev. Mod. Phys.* **76**, 323 (2004)
3. C.P. Bean, U.D. Livingston, Superparamagnetism. *J. Appl. Phys.* **30**, S120 (1959)
4. R. Wiesendanger, (ed) Atomic- and Nanoscale Magnetism. Springer International Publishing (2018)
5. R.H. Kodama, Magnetic nanoparticles. *J. Magn. Magn. Mater.* **200**, 359 (1999)
6. G. Reiss, A. Hütten, Applications beyond data storage. *Nat. Mater.* **4**, 725 (2005)
7. S.P. Gubin, (ed) Magnetic nanoparticles. Wiley (2009)
8. L. Mohammed, H.G. Gomaa, D. Ragab, J. Zhu, Magnetic nanoparticles for environmental and biomedical applications: A review. *Particuology* **30**, 1 (2017)
9. I.M. Anik, M.K. Hossain, I. Hossain, I. Ahmed, R.M. Doha, Biomedical applications of magnetic nanoparticles. In *Magnetic Nanoparticle-Based Hybrid Materials*. Woodhead Publishing, pp. 463–497 (2021)
10. Y. Xiao, J. Du, Superparamagnetic nanoparticles for biomedical applications. *J. Mater. Chem. B* **8**, 354 (2020)
11. S. Odenbach, ed., Ferrofluids: magnetically controllable fluids and their applications. Springer, p 594 (2008)
12. F. Almomani, R. Bhosale, M. Khraisheh, T. Almomani, Heavy metal ions removal from industrial wastewater using magnetic nanoparticles (MNP). *Appl. Surf. Sci.* **506**, 144924 (2020)
13. F.S.A. Khan, N.M. Mubarak, M. Khalid, R. Walvekar, E.C. Abdullah, S.A. Mazari, S. Nizamuddin, R.R. Karri, Magnetic nanoadsorbents' potential route for heavy metals removal-a review. *Environ. Sci. Pollut. Res.* **27**, 24342 (2020)
14. M.L. Seol, S.B. Jeon, J.W. Han, Y.K. Choi, Ferrofluid-based triboelectric-electromagnetic hybrid generator for sensitive and sustainable vibration energy harvesting. *Nano Energy* **31**, 233 (2017)
15. T. Dippong, E.A. Levei, F. Goga, I. Petean, A. Avram, O. Cadar, The impact of polyol structure on the formation of $\text{Zn}_{0.6}\text{Co}_{0.4}\text{Fe}_2\text{O}_4$ spinel-based pigments. *J. Sol-Gel Sci Technol* **92**, 736 (2019)
16. T. Dippong, E.A. Levei, C.L. Lengauer, A. Daniel, D. Toloman, O. Cadar, Investigation of thermal, structural, morphological and photocatalytic properties of $\text{Cu}_x\text{Co}_{1-x}\text{Fe}_2\text{O}_4$ ($0 \leq x \leq 1$) nanoparticles embedded in SiO_2 matrix. *Mater. Charact.* **163**, 110268 (2020)
17. V. Markovich, A. Wisniewski, H. Szymczak, Magnetic properties of perovskite manganites and their modifications. In *Handbook of Magnetic Materials*. Elsevier, vol. 22, 1 (2014)
18. W. Xia, Z. Pei, K. Leng, X. Zhu, Research progress in rare earth-doped perovskite manganite oxide nanostructures. *Nanoscale Res. Lett.* **15**, 1 (2020)
19. T. Zhang, X.P. Wang, Q.F. Fang, X.G. Li, Magnetic and charge ordering in nanosized manganites. *Appl. Phys. Rev.* **1**, 031302 (2014)
20. M.H. Phan, S. Chandra, N.S. Bingham, H. Srikanth, C.L. Zhang, S.W. Cheong, T.D. Hoang, H.D. Chinh, Collapse of charge ordering and enhancement of magnetocaloric effect in nanocrystalline $\text{La}_{0.35}\text{Pr}_{0.275}\text{Ca}_{0.375}\text{MnO}_3$. *Appl. Phys. Lett.* **97**, 242506 (2010)

21. X. Huang, T.R. Paudel, S. Dong, E.Y. Tsybmal, Hexagonal rare-earth manganites as promising photovoltaics and light polarizers. *Phys. Rev. B* **92**, 125201 (2015)
22. K. Knížek, Z. Jirak, E. Pollert, F. Zounova, S. Vratislav, Structure and magnetic properties of $\text{Pr}_{1-x}\text{Sr}_x\text{MnO}_3$ perovskites. *J. Solid State Chem.* **100**, 292 (1992)
23. D. Sánchez, J.A. Alonso, M.J. Martínez-Lope, Neutron-diffraction study of the Jahn-Teller transition in PrMnO_3 . *J. Chem. Soc. Dalton Trans.* **23**, 4422 (2002)
24. O. Chmaissem, B. Dabrowski, S. Kolesnik, J. Mais, J.D. Jorgensen, S. Short, Structural and magnetic phase diagrams of $\text{La}_{1-x}\text{Sr}_x\text{MnO}_3$ and $\text{Pr}_{1-y}\text{Sr}_y\text{MnO}_3$. *Phys. Rev. B* **67**, 094431 (2003)
25. W. Boujelben, M. Ellouze, A. Cheikh-Rouhou, J. Pierre, Q. Cai, W.B. Yelon, K. Shimizu, C. Dubourdieu, Neutron diffraction, NMR and magneto-transport properties in the $\text{Pr}_{0.6}\text{Sr}_{0.4}\text{MnO}_3$ perovskite manganite. *J. Alloys Compds.* **334**, 1 (2002)
26. D.V. Maheswar Repaka, T.S. Tripathi, M. Aparnadevi, R. Mahendiran, Magnetocaloric effect and magnetothermopower in the room temperature ferromagnet $\text{Pr}_{0.6}\text{Sr}_{0.4}\text{MnO}_3$. *J. Appl. Phys.* **112**, 123915 (2012)
27. C. Ritter, P.G. Radaelli, M.R. Lees, J. Baratt, G. Balakrishnan, D. McK Paul, A new monoclinic perovskite allotrope in $\text{Pr}_{0.6}\text{Sr}_{0.4}\text{MnO}_3$. *J. Solid State Chem.* **127**, 276 (1996)
28. A.D. Souza, M. Vagadia, M. Daivajna, Tuning magnetic and magnetocaloric properties of $\text{Pr}_{0.6}\text{Sr}_{0.4}\text{MnO}_3$ through size modifications. *J. Mater. Sci.: Mater. Electron.* **32**, 14990 (2021)
29. T. Atou, H. Chiba, K. Ohoyama, Y. Yamaguchi, Y. Syono, Structure determination of ferromagnetic perovskite BiMnO_3 . *J. Solid State Chem.* **145**, 639 (1999)
30. A. Dos Santos, A.K. Moreira, T. Cheetham, Y. Atou, Y. Syono, K. Yamaguchi, K. Ohoyama, H. Chiba, C.N.R. Rao, Orbital ordering as the determinant for ferromagnetism in biferroic BiMnO_3 . *Phys. Rev. B* **66**, 064425 (2002)
31. O.S. Mantyskaya, I.O. Troyanchuk, A.N. Chobot, H. Szymczak, Magnetic phase diagram of the manganites $\text{Bi}_{1-x}\text{Sr}_x\text{MnO}_3$. *Low Temp. Phys.* **30**, 218 (2004)
32. H. Chiba, T. Atou, Y. Syono, Magnetic and electrical properties of $\text{Bi}_{1-x}\text{Sr}_x\text{MnO}_3$: hole-doping effect on ferromagnetic perovskite BiMnO_3 . *J. Solid State Chem.* **132**, 139 (1997)
33. J.L. García-Muñoz, C. Frontera, M. Respaud, M. Giot, C. Ritter, X.G. Capdevila, Magnetic properties of $\text{Bi}_{0.75}\text{Sr}_{0.25}\text{MnO}_3$ ($x \approx 2/8$, $\text{TCO} = 600$ K): ferromagnetism and charge order. *Phys. Rev. B* **72**, 054432 (2005)
34. A.D. Souza, S. Rayaprol, M.S. Murari, Mamatha Daivajna, Structural, Magnetic and Magneto-transport properties of $\text{Bi}_{0.7-x}\text{La}_x\text{Sr}_{0.3}\text{MnO}_3$ Manganites. *Ceram. Int.* **47**, 1021 (2021)
35. N. Kambhala, M. Chen, L. Peng, X.X. Zhang, D. Rajesh, K.S. Bhagyashree, L.R. Goveas et al., Study of coexisting phases in Bi doped $\text{La}_{0.67}\text{Sr}_{0.33}\text{MnO}_3$. *J. Magn. Magn. Mater.* **406**, 22 (2016)
36. R.R. Zhang, G.L. Kuang, L.H. Yin, Y.P. Sun, Effect of progressive substitution of Bi^{3+} by La^{3+} on the structural, magnetic, and transport properties of $\text{Bi}_{0.6}\text{Ca}_{0.4}\text{MnO}_3$. *J. Appl. Phys.* **108**, 103903 (2010)
37. L. Righi, J. Gutierrez, J.M. Barandiaran, Structure, magnetic and transport properties in $\text{La}_{0.7-x}\text{Bi}_x\text{Ca}_{0.3}\text{MnO}_3$ perovskites. *J. Phys.: Condens. Matter* **11**, 2831 (1999)
38. M.D. Daivajna, N. Kumar, V.P.S. Awana, B. Gahtori, J. Benedict Christopher, S.O. Manjunath, K.Z. Syu, Y.K. Kuo, A. Rao, Electrical, magnetic and thermal properties of $\text{Pr}_{0.6-x}\text{Bi}_x\text{Sr}_{0.4}\text{MnO}_3$ manganites. *J. Alloys Compds.* **588**, 406 (2014)
39. M.D. Daivajna, A. Rao, W.J. Lin, Y.K. Kuo, Study of electrical and magnetic properties of $\text{Pr}_{0.6-x}\text{Bi}_x\text{Sr}_{0.4}\text{MnO}_3$ ($x = 0.20$ and 0.25). *Physica B: Condens. Matter* **514**, 54 (2017)
40. S.S. Pillai, P.N. Santhosh, N. Harish Kumar, P. John Thomas, F. Tuna, Cluster glass properties and magnetic phase separation studies of $\text{Nd}_x\text{Bi}_{0.5-x}\text{Sr}_{0.5}\text{MnO}_3$ ($x = 0.1, 0.2, 0.3$ and 0.4). *J. Phys.: Condens. Matter* **21**, 195409 (2009)
41. C. Shang, Z.C. Xia, B. Zhao, D.W. Liu, Y.Q. Wang, Y.L. Su, Effects of Bi^{3+} doping on charge ordering and high magnetic field phase diagram of $\text{Nd}_{0.6-x}\text{Bi}_x\text{Ca}_{0.4}\text{MnO}_3$. *Mater. Res. Bull.* **121**, 110611 (2020)
42. R. Seshadro, A. Nicola, Hill, Visualizing the role of Bi 6s “lone pairs” in the off-center distortion in ferromagnetic BiMnO_3 . *Chem. Mater.* **13**, 2892 (2001)
43. A.D. Souza, M.S. Murari, M.D. Daivajna, Structural, magnetic and magnetocaloric properties of Nanostructured $\text{La}_{0.5}\text{Bi}_{0.2}\text{Sr}_{0.3}\text{MnO}_3$ perovskites. *Physica B Condens. Matter* **580**, 411909 (2020)
44. J.R. Sun, J. Gao, Y. Fei, R.W. Li, B.G. Shen, Doping effects on the phase separation in perovskite $\text{La}_{0.67-x}\text{Bi}_x\text{Ca}_{0.33}\text{MnO}_3$. *Phys. Rev. B* **67**, 144414 (2003)
45. I. Kammoun, W. Cheikhrouhou-Koubaa, W. Boujelben, A. Cheikhrouhou, Structural and magnetic properties of Bi doped in the A site of $(\text{Pr}_{1-x}\text{Bi}_x)_{0.6}\text{Sr}_{0.4}\text{MnO}_3$ ($0 \leq x \leq 0.4$) perovskite manganites. *J. Mater. Sci.* **43**, 960 (2008)
46. A.D. Souza, S. Rayaprol, M.S. Murari, M. Daivajna, Effect of milling on structure and magnetism of nanocrystalline $\text{La}_{0.7-x}\text{Bi}_x\text{Sr}_{0.3}\text{MnO}_3$ ($x = 0.35, 0.40$) manganites. *Physica B Condens. Matter.* **606**, 412792 (2021)
47. A.D. Souza, S. Rayaprol, M. Daivajna, Effect of Bi^{3+} on magnetic properties of nanosized $\text{La}_{0.7-x}\text{Bi}_x\text{Sr}_{0.3}\text{MnO}_3$. *Mater Today Proc* (2021). <https://doi.org/10.1016/j.matpr.2020.11.765>
48. A.D. Souza, S. Rayaprol, M.S. Murari, M. Daivajna, Effect of Particle Size on Magnetic Phase Coexistence in Nanocrystalline $\text{La}_{0.4}\text{Bi}_{0.3}\text{Sr}_{0.3}\text{MnO}_3$ (Under Review)
49. T. Roisnel, J. Rodríguez-Carvajal, WinPLOTR: a windows tool for powder diffraction pattern analysis. *Mater. Sci. Forum* **378**, 118 (2001)
50. J. Rodríguez-Carvajal, T. Roisnel, Line broadening analysis using FullProf*: determination of microstructural properties. *Mater. Sci. Forum* **443**, 123 (2004)
51. M. Sopic-Lizer et al., High-energy ball milling: mechanochemical processing of nanopowders. Elsevier (2010)
52. J.S. Blázquez, J.J. Ipus, L.M. Moreno-Ramírez, J.M. Álvarez-Gómez, D. Sánchez-Jiménez, S. Lozano-Pérez, V. Franco, A. Conde, Ball milling as a way to produce magnetic and magnetocaloric materials: a review. *J. Mater. Sci.* **52**, 11834 (2017)
53. A. Pramothkumar, N. Senthilkumar, K. Jothivenkatachalam, Flake-like CuMn_2O_4 nanoparticles synthesized via co-precipitation method for photocatalytic activity. *Physica B Condens Matter* **572**, 117 (2019)
54. A.D. Souza, M. Vagadia, M. Daivajna, Effect of nanoscale size reduction on the magnetic properties of $\text{Pr}_{0.6}\text{Sr}_{0.4}\text{MnO}_3$. *J. Magn. Magn. Mater.* **538**, 168280 (2021)
55. A.D. Souza, S. Rayaprol, A. Sagdeo, A.K. Sinha, M. Daivajna, Magnetic phase transformation in $\text{La}_{0.7-x}\text{Bi}_x\text{Sr}_{0.3}\text{MnO}_3$ ($0.25 \leq x \leq 0.4$). *J. Magn. Magn. Mater.* **511**, 166966 (2020)
56. C. Kittel, *Introduction to Solid State Physics* (Wiley, New York, 1976)
57. A.K. Pramanik, A. Banerjee, Griffiths phase and its evolution with Mn-site disorder in the half-doped manganite $\text{Pr}_{0.5}\text{Sr}_{0.5}\text{Mn}_{1-y}\text{Ga}_y\text{O}_3$ ($y = 0.0, 0.025$, and 0.05). *Phys. Rev. B* **81**, 024431 (2010)
58. V.Y. Pomjakushin, D.V. Sheptyakov, E.V. Pomjakushina, K. Conder, A.M. Balagurov, Evidence for the strong effect of quenched correlated disorder on phase separation and magnetism in $(\text{La}_{1-y}\text{Pr}_y)_{0.7}\text{Ca}_{0.3}\text{MnO}_3$. *J. Phys. Condens Matter* **22**, 115601 (2010)
59. V. Markovich, R. Puzniak, I. Fita, A. Wisniewski, D. Mogilyansky, B. Dolgin, G. Gorodetsky, G. Jung, Irreversibility, remanence, and Griffiths phase in $\text{Sm}_{0.1}\text{Ca}_{0.9}\text{MnO}_3$ nanoparticles. *J. Appl. Phys.* **113**, 233911 (2013)

60. A.K. Pramanik, A. Banerjee, Finite-size effect on evolution of Griffiths phase in manganite nanoparticles. *J. Phys. Condens. Matter* **28**, 35LT02 (2016)
61. J.A. Souza, J.J. Neumeier, Yu. Yi-Kuo, Magnetic signatures of ferromagnetic polarons in $\text{La}_{0.7}\text{Ca}_{0.3}\text{MnO}_3$: Colossal magnetoresistance is not a Griffiths singularity. *Phys. Rev. B* **78**, 014436 (2008)
62. C.D. Batista, J. Eroles, M. Avignon, B. Alascio, Ferromagnetic polarons in manganites. *Phys. Rev. B* **62**, 15047 (2000)
63. J.A. Souza, Yu. Yi-Kuo, J.J. Neumeier, H. Terashita, R.F. Jardim, Method for analyzing second-order phase transitions: Application to the ferromagnetic transition of a polaronic system. *Phys. Rev. Lett.* **94**, 207209 (2005)
64. E. Rozenberg, M. Auslender, A.I. Shames, I. Felner, D. Mogilyansky, Y.M. Mukovskii, Griffith's phase versus chemical disorder in low-doped manganites: $\text{La}_{0.9}\text{Sr}_{0.1}\text{MnO}_3$ crystal revisited. *J. Appl. Phys.* **109**, 07D902 (2011)
65. E. Rozenberg, M. Auslender, I. Felner, A.I. Shames, G. Gorodetsky, Y.M. Mukovskii, Thermodynamics of paramagnetic-ferromagnetic phase transition in $\text{La}_{0.7}\text{Ca}_{0.3}\text{MnO}_3$ Manganite: "Griffiths singularity" versus Chemical Disorder and Lattice Effects. *IEEE Tran. Magn.* **46**, 1299 (2010)
66. A. Shahee, K. Singh, R.J. Choudhary, N.P. Lalla, Evidence of ferromagnetic short-range correlations in cubic $\text{La}_{1-x}\text{Sr}_x\text{MnO}_{3-\delta}$ ($x = 0.80, 0.85$) above antiferromagnetic ordering. *Phys. Status Solidi B* **252**, 1832 (2015)
67. B. Roy, A. Poddar, S. Das, Electrical transport properties and magnetic cluster glass behavior of $\text{Nd}_{0.7}\text{Sr}_{0.3}\text{MnO}_3$ nanoparticles. *J. Appl. Phys.* **100**, 104318 (2006)
68. B. Arun, M.V. Suneesh, M. Vasundhara, Comparative study of magnetic ordering and electrical transport in bulk and nano-grained $\text{Nd}_{0.67}\text{Sr}_{0.33}\text{MnO}_3$ manganites. *J. Magn. Magn. Mater.* **418**, 265 (2016)
69. N.D. Sharma, S. Sharma, N. Choudhary, M.K. Verma, D. Singh, Comparative study of $\text{La}_{0.5}\text{Nd}_{0.2}\text{Ca}_{0.3-x}\text{K}_x\text{MnO}_3$ ($x = 0.0$ and 0.05) nanoparticles: effect of A-cation size and calcination temperature. *Ceram. Int.* **45**, 13637 (2019)
70. B.D. Cullity, *Introduction to Magnetic Materials* (Addison-Wesley, MA, 1972)
71. A.D. Souza, P.D. Babu, S. Rayaprol, M.S. Murari, L.D. Mendonca, M. Daivajna, Size control on the magnetism of $\text{La}_{0.7}\text{Sr}_{0.3}\text{MnO}_3$. *J. Alloys Compd.* **797**, 874 (2019)
72. E.C. Devi, I. Soibam, Law of Approach to Saturation in Mn–Zn Ferrite Nanoparticles. *J. Supercond. Nov. Magn.* **32**, 1293 (2018)
73. D.H. Manh, P.T. Phong, T.D. Thanh, D.N.H. Nam, L.V. Hong, N.X. Phuc, Size effects and interactions in $\text{La}_{0.7}\text{Ca}_{0.3}\text{MnO}_3$ nanoparticles. *J. Alloys Compd.* **509**, 1373 (2011)
74. A.M. Tishin, Y.I. Spichkin, *The Magnetocaloric Effect and Its Applications* (CRC Press, USA, 2016)
75. H.N. Bez, H. Yibole, A. Pathak, Y. Mudryk, V.K. Pecharsky, Best practices in evaluation of the magnetocaloric effect from bulk magnetization measurements. *J. Magn. Magn. Mater.* **458**, 301 (2018)
76. A. Magnus, G. Carvalho, A.A. Coelho, P.J. Von Ranke, C.S. Alves, The isothermal variation of the entropy (ΔS_T) may be miscalculated from magnetization isotherms in some cases: MnAs and $\text{Gd}_3\text{Ge}_2\text{Si}_2$ compounds as examples. *J. Alloys Compd.* **509**, 3452 (2011)
77. J. Fan, L. Pi, L. Zhang, W. Tong, L. Ling, B. Hong, Y. Shi, W. Zhang, L. Di, Y. Zhang, Magnetic and magnetocaloric properties of perovskite manganite $\text{Pr}_{0.55}\text{Sr}_{0.45}\text{MnO}_3$. *Physica B: Condens. Matter* **406**, 2289 (2011)
78. S. Zemni, M. Baazaoui, H. Ja Dhahri, Vincent, and M. Oumezzine, Above room temperature magnetocaloric effect in perovskite $\text{Pr}_{0.6}\text{Sr}_{0.4}\text{MnO}_3$. *Mater. Lett.* **63**, 489 (2009)
79. M.D. Daivajna, A. Rao, Magnetocaloric effect in pristine and Bi-doped $\text{Pr}_{0.6}\text{Sr}_{0.4}\text{MnO}_3$ manganite. *Solid State Comm.* **245**, 65 (2016)
80. H. Biswal, V. Singh, R. Nath, J.R. Sahu, Magnetic properties and near-room-temperature large magnetocaloric effect in $(\text{La}_{1-x}\text{Bi}_x)_{0.67}\text{Ba}_{0.33}\text{MnO}_3$ ($x = 0-0.3$) ceramics. *Mater. Res. Bull.* **133**, 111030 (2021)
81. A. Elghoul, A. Krichene, N. Chniba Boudjada, W. Boujelben, Room temperature magnetocaloric effect in polycrystalline $\text{La}_{0.75}\text{Bi}_{0.05}\text{Sr}_{0.2}\text{MnO}_3$. *Appl. Phys. A* **125**, 780 (2019)
82. A.A. Khan, U. Hira, F. Sher, Large relative cooling power of Bi-doped $\text{La}_{0.8-x}\text{Bi}_x\text{Sr}_{0.08}(\text{Ca}_{0.55}\text{Ba}_{0.45})_{0.12}\text{MnO}_3$ ($x = 0.0, 0.1$ and 0.3) perovskites: magnetic and magnetocaloric properties. *Ceram. Int.* **43**, 7351 (2017)
83. N. Nedelko, S. Lewinska, A. Pashchenko, I. Radelytskyi, R. Diduszko, E. Zubov, W. Lisowski et al., Magnetic properties and magnetocaloric effect in $\text{La}_{0.7}\text{Sr}_{0.3-x}\text{Bi}_x\text{MnO}_3$ manganites. *J. Alloys Compd.* **640**, 433 (2015)
84. A. Kharrat, B. Jazia, E.K. Hlil, W. Boujelben, Bi doping effect on the critical behavior and magnetocaloric effect of $\text{Pr}_{0.8-x}\text{Bi}_x\text{Sr}_{0.2}\text{MnO}_3$ ($x = 0, 0.05$ and 0.1). *J. Alloys Compd.* **739**, 101 (2018)
85. W. Mabrouki, A. Krichene, N.C. Boudjada, W. Boujelben, Sintering temperature effect on the magnetic properties of $\text{Pr}_{0.67}\text{Sr}_{0.33}\text{MnO}_3$ manganite. *Appl. Phys. A* **126**, 1 (2020)
86. H. Baaziz, A. Tozri, E. Dhahri, E.K. Hlil, Effect of particle size reduction on the structural, magnetic properties and the spin excitations in ferromagnetic insulator $\text{La}_{0.9}\text{Sr}_{0.1}\text{MnO}_3$ nanoparticles. *Ceram. Int.* **41**, 2955 (2015)
87. M. Bourouina, A. Krichene, N.C. Boudjada, M. Khitouni, W. Boujelben, Structural, magnetic and magnetocaloric properties of nanostructured $\text{Pr}_{0.5}\text{Sr}_{0.5}\text{MnO}_3$ manganite synthesized by mechanical alloying. *Ceram. Int.* **43**, 8139 (2017)
88. V.M. Andrade, R.J. Caraballo Vivas, S.S. Pedro, J.C.G. Tedesco, A.L. Rossi, A.A. Coelho, D.L. Rocco, M.S. Reis, Magnetic and magnetocaloric properties of $\text{La}_{0.6}\text{Ca}_{0.4}\text{MnO}_3$ tunable by particle size and dimensionality. *Acta Mater.* **102**, 49 (2016)
89. T. Dipping, O. Cadar, I.G. Deac, M. Lazar, G. Borodi, E.A. Levei, Influence of ferrite to silica ratio and thermal treatment on porosity, surface, microstructure and magnetic properties of $\text{Zn}_{0.5}\text{Ni}_{0.5}\text{Fe}_2\text{O}_4/\text{SiO}_2$ nanocomposites. *J. Alloys Compd.* **828**, 154409 (2020)
90. T. Dipping, E.A. Levei, I.G. Deac, F. Goga, O. Cadar, Investigation of structural and magnetic properties of $\text{Ni}_x\text{Zn}_{1-x}\text{Fe}_2\text{O}_4/\text{SiO}_2$ ($0 \leq x \leq 1$) spinel-based nanocomposites. *J. Anal. Appl. Pyrolysis* **144**, 104713 (2019)
91. Q. Li, C.W. Kartikowati, S. Horie, T. Ogi, T. Iwaki, K. Okuyama, Correlation between particle size/domain structure and magnetic properties of highly crystalline Fe_3O_4 nanoparticles. *Sci. Rep.* **7**, 1 (2017)
92. R.S. Yadav, J. Havlica, M. Hnatko, P. Šajgalík, C. Alexander, M. Palou, E. Bartoníčková et al., Magnetic properties of $\text{Co}_{1-x}\text{Zn}_x\text{Fe}_2\text{O}_4$ spinel ferrite nanoparticles synthesized by starch-assisted sol-gel auto combustion method and its ball milling. *J. Magn. Magn. Mater.* **378**, 190 (2015)
93. M.A. Lopez-Quintela, L.E. Hueso, J. Rivas, F. Rivadulla, Intergranular magnetoresistance in nanomanganites. *Nanotechnology* **14**, 212 (2003)
94. T.A. Ho, T.D. Thanh, S.K. Oh, S.C. Yu, Effect of crystallite size on the thickness of nonmagnetic shell and magnetic properties of $\text{La}_{0.7}\text{Ca}_{0.3}\text{MnO}_3$. *J. Supercond. Nov. Magn.* **28**, 891 (2015)